INSTRUMENT ARTIFACTS LEAD TO UNCERTAINTIES IN PARAMETERIZATIONS OF CLOUD CONDENSATION NUCLEATION

A Thesis

by

JESSICA AILEEN MIRRIELEES

Submitted to the Office of Graduate and Professional Studies of
Texas A&M University
in partial fulfillment of the requirements for the degree of

MASTER OF SCIENCE

Chair of Committee,	Sarah D. Brooks
Co-Chair of Committee,	Daniel C.O. Thornton
Committee Members,	Donald R. Collins
	Gunnar Wolfgang Schade
	Renyi Zhang
Head of Department,	Ping Yang

August 2018

Major Subject: Atmospheric Sciences

ABSTRACT

The concentrations of cloud condensation nuclei (CCN) modulate cloud properties, rainfall location and intensity, and climate forcings. This work assesses uncertainties in CCN measurements and the apparent hygroscopicity parameter (κ_{app}) which is widely used to represent CCN populations in climate models. CCN measurements require accurate operation of three instruments: the CCN instrument, the differential mobility analyzer (DMA), and the condensation particle counter (CPC). Assessment of DMA operation showed that varying the ratio of aerosol to sheath flow from 0.05 to 0.30 resulted in discrepancies between the κ_{app} values calculated from CCN measurements and the literature values. Discrepancies were found to increase from effectively zero to 0.18 for sodium chloride, and from effectively zero to 0.08 for ammonium sulfate. The ratio of excess to sheath flow was also varied, which shifted the downstream aerosol distribution towards smaller particle diameters (for excess flow < sheath flow) or larger particle diameters (for excess flow > sheath flow) than predicted. For the CPC instrument, undercounting occurred at high concentrations, resulting in calculated κ_{app} lower than the literature values. Lastly, undercounting by CCN instruments at high concentration was also assessed, taking the effect of supersaturation on counting efficiency into account. Under recommended operating conditions, the combined DMA, CPC, and CCN uncertainties in κ_{app} are 1.1 % or less for 25 to 200 nm diameter aerosols.

ACKNOWLEDGEMENTS

I would like to thank my committee chair, Dr. Brooks, my committee co-chair, Dr. Thornton, and my committee members, Dr. Zhang, Dr. Collins, and Dr. Schade, for their guidance and support throughout the course of this research.

Thanks also go to my friends and colleagues and the department faculty and staff for making my time at Texas A&M University a great experience.

CONTRIBUTORS AND FUNDING SOURCES

This work was supervised by a thesis committee consisting of Dr. Brooks, Dr. Collins, Dr. Zhang, and Dr. Schade of the Department of Atmospheric Sciences, and Dr. Thornton of the Department of Oceanography. All work for the dissertation was completed independently by the student.

This project was supported by the National Science Foundation of the United States (Award #15398810). Graduate study was supported by a fellowship from the Hagler Institute for Advanced Study at Texas A&M University and a Lechner Scholarship.

NOMENCLATURE

a, b	Köhler theory constants
$\alpha_{CC}, \beta_{CC}, \gamma_{CC}$	Empirically-determined Cunningham slip correction factor constants
Z_p	Aerosol particle electrical mobility
C_C	Cunningham slip correction factor
d_m	Electrical mobility diameter
n	Number of charges on particle
λ	Mean free path
Q_{sh}	Sheath flow
Q_e	Excess air flow
Q_a	Aerosol flow
Q_s	Sample flow
κ_{app}	Apparent hygroscopicity parameter
$\kappa_{app,artifact}$	Apparent hygroscopicity parameter artifact
s	Equilibrium water vapor saturation
s_{crit}	Critical saturation (50 % of aerosols active as cloud condensation nuclei)
A	Constant used in calculating κ_{app}
σ_{lv}	Surface tension of water
T	Temperature
D_{act}	Activation diameter
SS_{crit}	Critical percent supersaturation

α_{TF}	Height of DMA transfer function
β_{TF}	Half-width of DMA transfer function
Z_p'	Mobility of particle at DMA inlet
$Z_{p,mid}$	Midpoint of transfer function
ΔZ_p	Half-width of transfer function
V_0	Voltage selected at DMA
r_1	DMA inner radius
r_2	DMA outer radius
L	DMA length
d_{50}	50 %-cut-off diameter

TABLE OF CONTENTS

Page

LIST OF FIGURES

Page

LIST OF TABLES

Page

1. INTRODUCTION

Aerosol-cloud interactions represent a major uncertainty in current predictions of the Earth's climate (IPCC 2013). According to well-known Köhler theory, an aerosol's potential to catalyze cloud droplet formation by activating as a cloud condensation nucleus (CCN) depends on its physical and chemical properties. For any given composition, the CCN activation potential of an aerosol increases as its diameter decreases. While the relationship between aerosol diameter and CCN activation is straightforward, the effect of composition on an aerosol's ability to participate in cloud formation is more complex (Petters and Kreidenweis 2013, Ovadnevaite et al. 2011) Predicting the cloud forming capacity of various air masses based on the properties of the aerosol they contain is essential for evaluating relative contributions from pollution, continental background and marine aerosol sources (Brooks and Thornton 2018, Carslaw et al. 2013). Long-term CCN measurements are available from numerous locations globally (Schmale et al. 2018). However, understanding regional and temporal variability in CCN populations requires the ability to assess whether observed differences reflect true physical differences or simply variations in CCN sampling strategies.

Parameterizations of CCN activity which accurately prescribe CCN measurements are needed for climate models, cloud resolving models, and air quality predictions (Betancourt, Nenes, and Liu 2013, Betancourt and Nenes 2014, Chang et al. 2017, Crosbie et al. 2015, Karydis et al. 2012, Kawecki and Steiner 2018). One parameterization was designed to represent the cloud droplet activation potential ambient aerosol masses of unknown composition with a single variable, kappa (κ) based on the dry aerosol's hygroscopicity, or ability to uptake water and form

a solution droplet (Petters and Kreidenweis 2007). Various names and abbreviations have been given to κ throughout the literature: "hygroscopicity parameter", "single hygroscopicity parameter", κ (Petters and Kreidenweis 2007, Carrico et al. 2008, Asa-Awuku et al. 2010, Moore et al. 2012); "CCN-derived κ", κ_{CCN} (Carrico et al. 2008, Petters and Kreidenweis 2007); and the "apparent hygroscopicity parameter" κ_{app} (Sullivan et al. 2009, Collins et al. 2016, Petters and Kreidenweis 2013). The term *apparent* hygroscopicity is favored by many because it emphasizes the fact that while CCN activation can often be predicted accurately by hygroscopic water uptake, they are different physical processes. It is possible for a compound to have high intrinsic hygroscopicity and low apparent hygroscopicity if it is poorly soluble in water (Sullivan et al. 2009).

Once calculated, hygroscopicity parameters are useful tools for comparing CCN field measurements conducted in various regions and seasons and for making predictions about cloud formation, aerosol-cloud interactions in weather, and climate models. Values of κ_{app} can be used to compare the CCN results in field and laboratory studies, including sea spray aerosol. For example, aggregation of results from several mesocosm experiments and marine field studies found submicron (30-100 nm) κ_{app} for sea spray aerosol as low as 0.4 and as high 1.3 (Collins et al. 2016).

Several studies have examined the sensitivity of models to κ values derived from HTDMA (humidified tandem differential mobility analyzer) measurements. An analysis of the NASA Global Modeling Initiative Chemical Transport Model and the GEOS-Chem CTM (Karydis et al.

2012) found that cloud droplet number concentration is sensitive to κ in Arctic and remote regions, where background aerosol loadings are low. Another study (Betancourt and Nenes 2014) found that a ±50 % uncertainty range in the κ of secondary organic aerosols and particulate organic matter resulted in a cloud droplet number concentration uncertainty of up to 15 % and 16 %, respectively. Updating precipitation models with lab-derived κ values for specific inorganic and organic species may increase the accuracy of storm forecasts by providing better predictions of intense precipitation (Kawecki and Steiner 2018). In terms of climate, (Liu and Wang 2010) found that increasing the κ of primary organic aerosols from 0 to 0.1, and decreasing the κ of secondary organics aerosols from 0.14 to 0.07, resulted in an uncertainty in global secondary aerosol indirect forcing of 0.4 Wm^{-2} from pre-industrial times to present day.

The sensitivity of weather and climate models to hygroscopicity parameters demonstrates the need for accurate measurements. In this study, we examine experimental uncertainties in CCN measurements and the resulting uncertainties in determination of κ_{app}. Differences in reported κ_{app} values may result from experimental artifacts rather any actual differences in aerosol's ability to facilitate cloud formation. By systematically quantifying sources of experimental error, this study provides a framework for determining the significance of variations in CCN properties reported in multiple studies and defining the operating conditions which minimize instrumental artifacts.

2. BACKGROUND

The Köhler equation relates water vapor saturation at the surface of a wet droplet, s, to its radius at equilibrium (Rogers and Yau 1989):

$$s = \left(1 - \frac{b}{r^3}\right) \exp\left(\frac{a}{r}\right) \tag{1a}$$

where a and b are constants derived from physical properties of water and a solvent:

$$a = \frac{2\sigma_w M_w}{\rho_w RT} \tag{1b}$$

$$b = \frac{3im_s M_w}{4\pi\rho_w M_s} \tag{1c}$$

where s is the equilibrium saturation ratio of a solution droplet with radius r, σ_w is the surface tension of water, M_w is the molecular weight of water, R is the ideal gas constant, T is temperature in Kelvin, ρ_w is the density of water, and M_s is the molecular weight of the solute. The minimum saturation ratio that is required for spontaneous droplet growth, s_{act}, is therefore:

$$s_{crit} = 1 + \sqrt{\frac{4a^3}{27b}} \tag{2}$$

Petters and Kreidenweis [2007] reformulated the Köhler equation as κ-Köhler theory:

$$s_{crit} = exp\left(\sqrt{\frac{4A^3}{27D_{act}^3\kappa_{app}}}\right) \quad (3a)$$

where A is a constant derived from the physical properties of water:

$$A = \frac{4\sigma_{lv}M_w}{RT\rho_w} \quad (3b)$$

where s_{crit} is the critical water vapor saturation, D_{act} is the dry particle activation diameter and κ_{app} is the apparent hygroscopicity parameter. Solving for κ_{app} yields:

$$\kappa_{app} = \frac{4A^3\sigma_{lv}^3}{27T^3D_{act}^3ln^2(s_{crit})} \quad (4)$$

The apparent hygroscopicity parameter can be calculated from experimental CCN results, where the dry diameter and water vapor saturation are known. For a chosen aerosol diameter, the activated fraction is the ratio of the concentration aerosols that activate as CCN to the total aerosol concentration:

$$Activated\ fraction = \frac{CCN\ Concentration}{Aerosol\ Concentration} \quad (5)$$

Activated fraction data is fit with a sigmoid error function to determine the supersaturation at which 50 % of the particles have activated as CCN, which is considered the operationally

defined critical supersaturation SS_{crit} (Rose et al. 2008). The critical saturation s_{crit} can then be determined and entered into Eq. (4) in order to calculate κ_{app} for the near-monodisperse aerosol:

$$s_{crit} = 1 + \frac{SS_{crit}}{100} \tag{6}$$

Reporting κ_{app} as a function of diameter allows for the comparison of the cloud condensation nucleation abilities of multimodal aerosol populations, without overlooking differences which arise due to aerosol composition.

The apparent hygroscopicity parameter is related to chemical composition; therefore, the calculated κ_{app} of a pure substance should be constant across CCN experiments. However, discrepancies between κ_{app} for a single chemical species have been observed. Experimental results for ammonium nitrate are inconsistent $0.577 \leq \kappa_{app} \leq 0.753$, and large ranges are often observed for organic compounds, such as glutaric acid ($0.054 \leq \kappa_{app} \leq 0.16$) and malonic acid ($0.199 \leq \kappa_{app} \leq 0.255$) (Koehler et al. 2006, Kumar, Broekhuizen, and Abbatt 2003, Hartz et al. 2006, Svenningsson et al. 2006). Below we evaluate potential sources of uncertainties in CCN measurements and the resulting uncertainties in κ_{app}.

3. ARTIFACTS FROM CCN MEASUREMENTS

3.1 Artifacts Derived from Differential Mobility Analyzers

CCN measurements require accurate operation of three instruments: the CCN, the differential mobility analyzer (DMA), and the condensational particle counter (CPC). The setup for laboratory CCN experiments is shown in Fig. 1. First, a polydisperse population of aerosols is generated by an atomizer and dried using a desiccant tube packed with silica gel. A near-monodisperse flow is obtained through size-selection in the DMA. The flow is then split between a CPC (which measures aerosol concentration) and a CCN counter (which measures the concentration of particles that activate as cloud condensation nuclei at a given percent water vapor supersaturation).

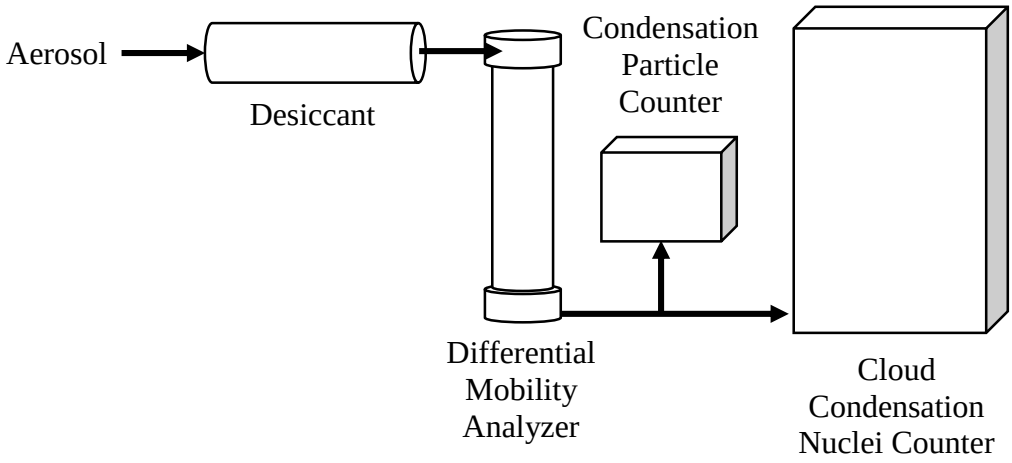

Figure 1 Experimental setup for CCN measurements

3.1.1 DMA Operation and Electrical Mobility

Differential mobility analyzers used in atmospheric science include commercially available instruments from Grimm Aerosol Technik, TSI Incorporated, and MSP Corporation. They have also been custom built by a number of research groups (Mei, Fu, and Chen 2011, Barmpounis et al. 2016, Jokinen and Makela 1997, Seol et al. 2000). All models allow for the selection of particles through electrical mobility, the ability of a particle to move through a medium (such as air) while acted upon by an electrical field. The DMA size-selects near-monodisperse aerosol from a polydisperse aerosol source, as shown in Fig. 2 (modeled after the Vienna-type long Differential Mobility Analyzer from Grimm Technologies).

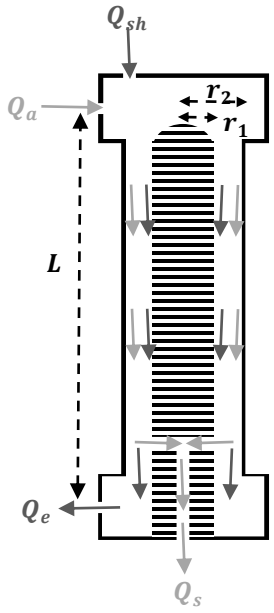

Figure 2 Simplified flow diagram of a DMA
The radius of the inner electrode is r_1, the radius of the outer electrode is r_2, and the distance between aerosol inlet and sample outlet is L. Q_{sh} represents the clean sheath air flow, Q_a represent the aerosol flow, Q_e represents the excess air flow, and Q_s represents the sample air flow.

The electrical mobility Z_p of a particle with mobility diameter d_m can be calculated according to:

$$Z_p = \frac{neC_C(d_m)}{3\pi\eta d_m} \tag{7}$$

where n is the number of charges on the particle (assumed to be one in this study), e is the elementary unit of charge, η is the gas dynamic viscosity, and $C_C(d_m)$ is the Cunningham slip correction factor:

$$C_C(d_m) = 1 + \frac{2\lambda}{d_m}\left(\alpha_{CC} + \beta_{CC} \exp\left[-\frac{\gamma_{CC}}{2\lambda/d_m}\right]\right) \tag{8}$$

where λ is the mean free path (DeCarlo et al. 2004). For the Vienna-type long Differential Mobility Analyzer from Grimm Technologies, Inc. considered here, $\alpha_{CC} = 1.246$, $\beta_{CC} = 0.42$, and $\gamma_{CC} = 0.86$ (Grimm Aerosol Technik, 2009).

Particle-laden flow enters the differential mobility analyzer through the aerosol inlet (flow Q_a), and travels down the DMA column (inner radius r_1, outer radius r_2) with the clean air sheath flow Q_{sh}. Positively-charged particles are attracted by the negatively-charged inner electrode, to which voltage V_0 has been applied. Ideally, selection of a voltage allows only particles of a specific mobility diameter to exit the DMA through the sample flow Q_s. All particles with larger diameter (lower Z_p) or smaller diameter (higher Z_p) will exit the DMA through the excess flow Q_e. In other words, Q_s would ideally be a truly monodisperse flow.

In reality, the aerosol flow that leaves the DMA through Q_s is polydisperse with a mobility distribution determined by instrumental parameters. A triangular approximation has been chosen as a model for this distribution, as particle inertia is negligible for the diameters considered in this study (Stratmann et al. 1997, Mamakos, Ntziachristos, and Sarnaras 2007). The probability that a particle at the aerosol inlet will exit with the sampling flow is defined by transfer function $f\left(Z_p, Z_{p,mid}\right)$:

$$f\left(Z_p, Z_{p,mid}\right) = \frac{\alpha_{TF}}{2\beta_{TF}}\left(\left|\frac{Z_p}{Z_{p,mid}} - (1+\beta_{TF})\right| + \left|\frac{Z_p}{Z_{p,mid}} - (1-\beta_{TF})\right| - 2\left|\frac{Z_p}{Z_{p,mid}} - 1\right|\right) \quad (9)$$

where $Z_{p,mid}$ is the midpoint mobility of the transfer function, and α_{TF} and β_{TF} are flow-derived constants, defined as:

$$\alpha_{TF} = \frac{Q_s + Q_a}{2Q_a} \quad (10a)$$

and

$$\beta_{TF} = \frac{Q_s}{Q_{sh}} \quad (10b)$$

The midpoint and half-width of the transfer function are respectively calculated according to (Knutson and Whitby 1975):

$$Z_{p,mid} = \frac{Q_e + Q_{sh}}{4\pi L V_0} \ln\left(\frac{r_2}{r_1}\right) \quad (11a)$$

and

$$\Delta Z_p = \frac{Q_a}{2\pi L V_0} \ln\left(\frac{r_2}{r_1}\right) \quad (11b)$$

3.1.2 κ_{app} Artifact Analysis and Results

Next we assess the ramifications of the DMA transfer function for the derived κ_{app}. A lognormal theoretical aerosol number distribution was used to represent a polydisperse ambient aerosol population (Fig. 3a). This distribution was converted to an electrical mobility distribution using Eq. (7) and Eq. (8), assuming that the aerosols in the distribution were spherical and singly charged. From the distribution, a series of single aerosol sizes were selected (25, 50, 100, and 200 nm diameter). For each aerosol size, the resulting DMA transfer functions were calculated for 7 cases using Eq. (9) and the various parameters for DMA sheath, excess, aerosol, and sample flow listed in Table 1. For example, the resulting DMA transfer functions for a 100 nm aerosol conditions constrained by Cases 1-4 are shown in Fig. 3b, where an increase in Q_a/Q_{sh} from 0.1 (black line) to 0.3 (green line) tripled the width of the number distribution, and decreasing Q_a/Q_{sh} to 0.05 (blue line) from 0.10 halved the width of the number distribution. The result of applying the transfer functions shown in Fig. 3b to the distribution in Fig. 3a is shown in Fig. 3c.

Table 1 Theoretical DMA Flow Test Cases

Case	Q_{sh} (L/min)	Q_e (L/min)	Q_a (L/min)	Q_s(L/min)	Q_a/Q_{sh}	Q_e/Q_{sh}
DMA 1	3	3	0.3	0.3	0.1	1
DMA 2	3	3	0.15	0.15	0.05	1
DMA 3	3	3	0.6	0.6	0.2	1
DMA 4	3	3	0.9	0.9	0.3	1
DMA 5	3	3.06	0.36	0.3	0.12	1.02
DMA 6	3	3.15	0.45	0.3	0.15	1.05
DMA 7	3	2.94	0.24	0.3	0.08	0.98

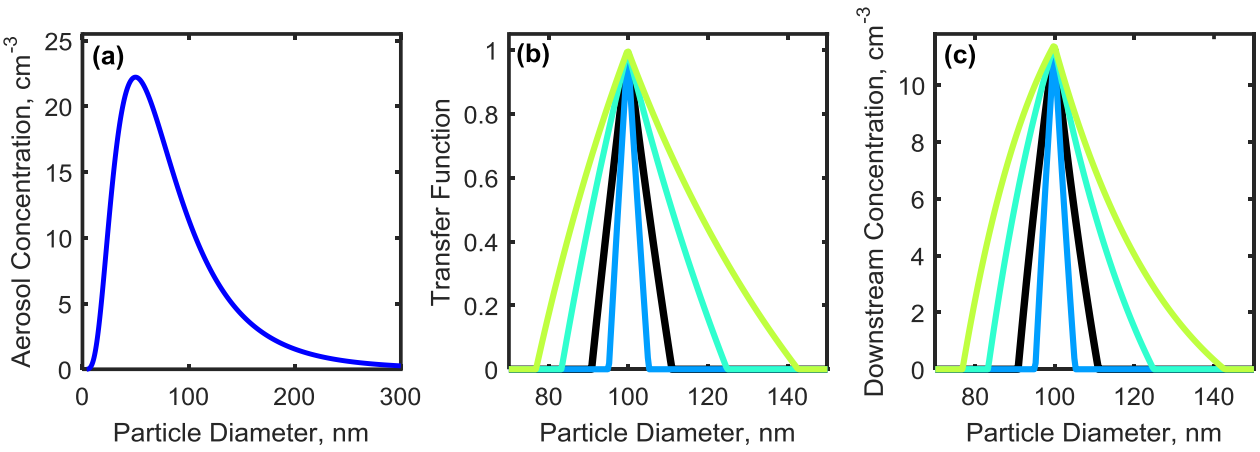

Figure 3 Transfer function example
(a) A theoretical aerosol distribution generated using a lognormal function centered at 50 nm. The total concentration for this distribution is 2000 particles/cm^3. (b) The transfer function calculated using Eq. (7). (c) Downstream aerosol concentration, cm^{-3} (Distribution x transfer function = downstream concentration).

All downstream distributions for all seven DMA cases and all aerosol sizes are shown in Fig. A-1 in the Appendix. DMA Cases 1-4 represent experimental conditions in which the sheath and excess air flows are equal and the aerosol/sheath flow ratio is varied. As Q_a/Q_{sh} increases, the width of the number distribution measured downstream of the DMA increases, while the midpoint diameter remains constant. It was found that doubling the aerosol to sheath ratio doubled the width of the downstream number distribution for 25, 50, 100, and 200 nm particles. For example, when selecting 200 nm particles, increasing Q_a/Q_{sh} from 0.10 to 0.20 increased the downstream diameter range from 181-222 nm (a spread of 41 nm) to 167-250 nm (a spread of 87 nm). The particle diameter ranges that would be observed downstream of the DMA are summarized in Table 2.

Table 2 Predicted downstream particle diameter range for each DMA case

Case	25 nm	50 nm	100 nm	200 nm
DMA 1	23-27	46-56	91-111	181-222
DMA 2	24-26	48-53	95-105	190-211
DMA 3	21-31	42-62	83-125	167-250
DMA 4	20-36	39-71	77-143	154-285
DMA 5	23-27	45-55	90-110	181-220
DMA 6	22-27	45-54	89-107	178-215
DMA 7	23-28	46-56	92-112	183-225

To assess the variations in CCN properties resulting from DMA uncertainties the critical supersaturation were calculated for representative atmospheric aerosols. The value of SS_{crit} was calculated for each particle diameter using Eq. (3a), using literature values for apparent hygroscopicity of 0.61 for ammonium sulfate and 1.28 for sodium chloride (Clegg, Brimblecombe, and Wexler 1998). It should be noted that this analysis considers two homogeneous aerosol distributions of hygroscopic salts. Real aerosol distributions tend to be mixtures of many species, and the shape of the number distribution can vary between species.

Note that in the absence of DMA diameter uncertainty, this single component aerosol population should be characterized by a single κ_{app} regardless of diameter. To test how uncertainties in DMA diameter translate to uncertainties in κ_{app}, the true critical saturation ratio s_{crit} was then put into Eq. (4) in order to calculate the "perceived" κ_{app} for each diameter given the chosen transfer function from Cases 1-7. For example, if 100 nm particles were selected from the DMA by the user, the transfer functions would allow larger and smaller particles to pass into the sample flow, as shown in Table 2. Particles with diameter > 100 nm would be "perceived" to have higher apparent hygroscopicity than particles with diameter < 100 nm, since the equilibrium vapor pressure over the surface of a particle decreases as its diameter increases (and as curvature

decreases). Using Eq. (12), these diameter-specific "perceived" κ_{app} values were volume-weighted, resulting in $\kappa_{app,theory}$:

$$\kappa_{app,theory} = \sum_i \epsilon_i \kappa_i \quad (12)$$

Results for ammonium sulfate and sodium chloride are shown in Fig. 4a. The critical saturation ratio was calculated from $\kappa_{app,theory}$ using Eq. (3a) for each case and converted to critical supersaturation. The results are compared to theoretical κ-Köhler theory curves for ammonium sulfate and sodium chloride generated using the literature κ_{app} for each compound (Fig. 4b).

Discrepancies between $\kappa_{app,theory}$ calculated in this study and literature values (hereon referred to as "κ_{app} artifacts") are shown for both compounds in Fig. 4c-d.

The greatest κ_{app} artifacts were found in DMA case 4 (where the aerosol/sheath ratio was the highest) for both ammonium sulfate and sodium chloride aerosols. The artifacts for ammonium sulfate in DMA case 4 were 0.05-0.08, or 8-13 % of the literature value used for $\kappa_{app}^{(NH_4)_2SO_4}$, while the sodium chloride artifacts in DMA case 4 were 0.11-0.18, or 9-14 % of the literature value used for κ_{app}^{NaCl}. Artifacts were also high for DMA case 6 ($-0.025 \leq \kappa_{app,artifact}^{(NH_4)_2SO_4} \leq -0.018$) and DMA case 7 ($0.016 \leq \kappa_{app,artifact}^{(NH_4)_2SO_4} \leq 0.017$), where $Q_e > Q_{sh}$.

κ_{app} artifacts were larger for sodium chloride ($-0.05 \leq \kappa_{app,artifact}^{NaCl} \leq 0.18$,4 − 14 % of κ_{app}^{NaCl}) than for ammonium sulfate ($-0.03 \leq \kappa_{app,artifact}^{(NH_4)_2SO_4} \leq 0.08$, 5 − 13 % of $\kappa_{app}^{(NH_4)_2SO_4}$) across the DMA cases. As our results show, when two or more compounds are compared, the more hygroscopic compound will have larger κ_{app} artifacts.

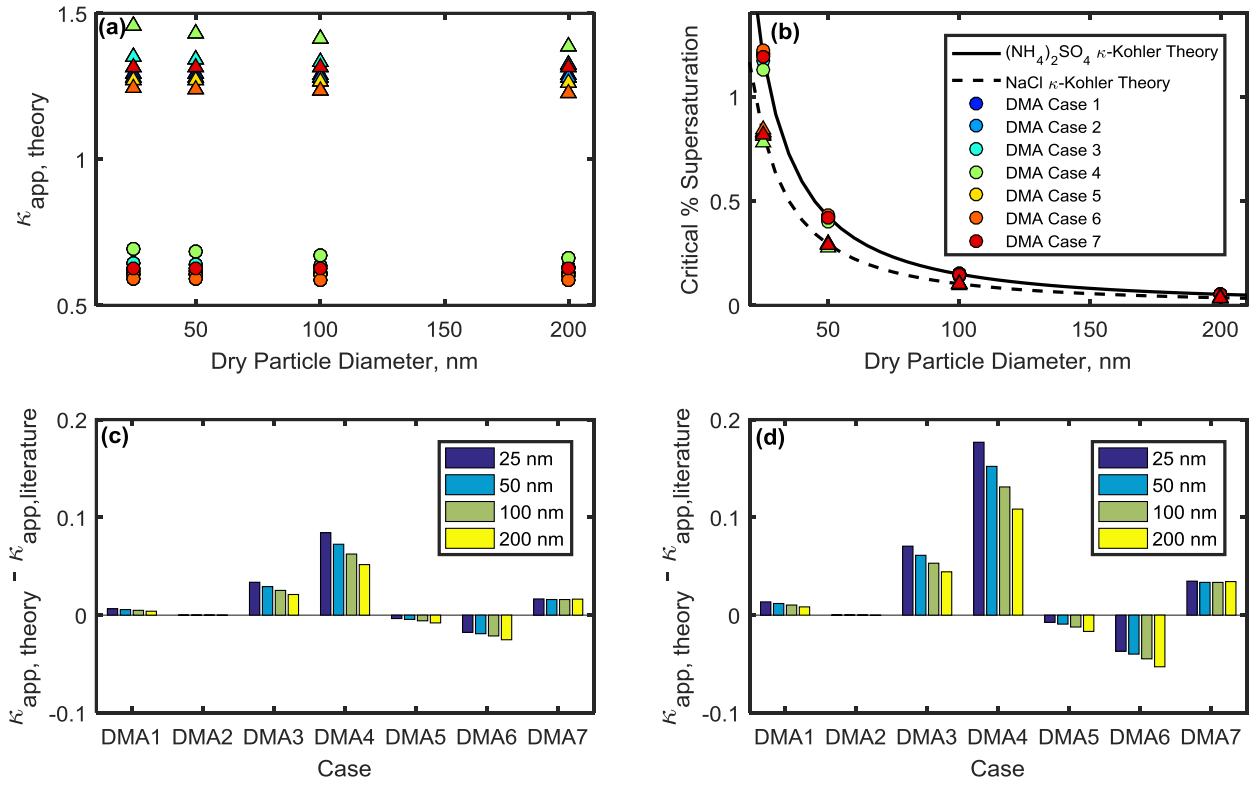

Figure 4 DMA case results

(a) Apparent hygroscopicity κ_{app} for each DMA case. Triangles represent the results for sodium chloride, and circles represent the results for ammonium sulfate; only one is shown in (b) to conserve space. (b) The critical supersaturation of ammonium sulfate and sodium chloride particles calculated for Cases 1-7 using κ_{app} values derived in (a). Ammonium sulfate and sodium chloride curves from κ-Köhler theory are shown for comparison. (c,d) DMA-flow-derived artifacts in κ_{app} for ammonium sulfate are shown for each DMA case for ammonium sulfate aerosols and sodium chloride aerosols.

4. ARTIFACTS DERIVED FROM CONDENSATIONAL PARTICLE COUNTERS

4.1 CPC Operation at Low Concentration

The second instrument which must function accurately during CCN experiments is the condensation particle counter. CPC performance is characterized by the maximum counting efficiency (which may be influenced by the working fluid in the instrument) and the 50 %-cut-off diameter (d_{50}), the particle diameter at which 50 % counting efficiency is observed, both of which can vary between commercially available models and even between individual CPCs (Heim et al. 2004). One study found that n-butanol CPCs (TSI, Inc. Models 3772, 3775, and 3776) exhibited smaller d_{50} for silver particles than sodium chloride ($3.3\ nm \leq d_{50}^{Ag} \leq 7.8\ nm$ and $4.1\ nm \leq d_{50}^{NaCl} \leq 14.7\ nm$), due to the more effective condensation of n-butanol on silver particles (Hermann et al. 2007).

Maximum counting efficiencies in that study varied from 88.9 % to 100.3 %. Another comparison of n-butanol CPCs (TSI Inc. Models 3010 and 3022, Grimm Tech. Inc. Model 5.403) found $3.1\ nm \leq d_{50} \leq 11.9\ nm$ for sodium chloride aerosols (Heim et al. 2004). In another study, the counting efficiencies observed in measurements of tungsten oxide particles by different instruments of the same model (TSI 3025) varied from 88.9 % to 138.9 %, while $d_{50}^{WO_x}$ varied from 3.2 nm to 11.0 nm (Hameri, O'Dowd, and Hoell 2002).

While some issues can cause undercounting at all concentrations, the additional issue of uncounted particles due to the arrival of more than one particle in the detector's field of view at any time arises only at higher concentrations. The cut-off between "low" and "high" concentration is not exact and varies between instruments. CPC undercounting issues which arise even at relatively low concentrations will be discussed in this section, and concentration-dependent effects will be explored in Sect. 4.2.

Six counting efficiency curves were generated using sigmoidal distributions and the 50 % cut-off diameters and maximum counting efficiencies listed in Table 3. Chosen values represent d_{50} values and maximum counting efficiencies reported in the literature under relatively low concentrations of 1000-4000 cm^{-3} (Hermann et al. 2007). The resulting sigmoidal distributions (Fig. 5a) were used to determine the counting efficiency of 25, 50, 100, and 200 nm particles.

Table 3 Parameters used in investigating κ_{app} artifacts for low concentrations measured by a condensation particle counter

Case	$\boldsymbol{d_{50}}$, nm	Maximum Counting Efficiency
CPC 1	15	100 %
CPC 2	10	100 %
CPC 3	5	100 %
CPC 4	10	90 %
CPC 5	10	95 %
CPC 6	10	98 %

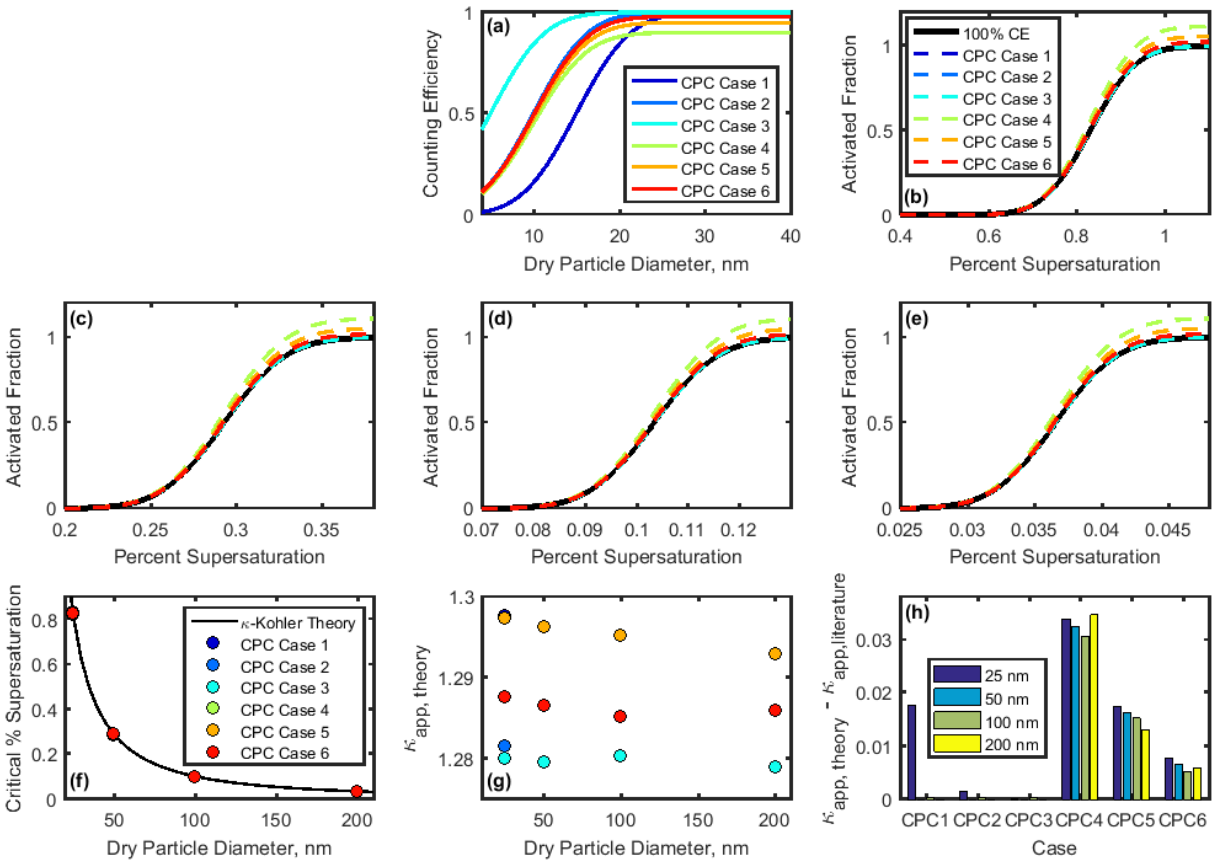

Figure 5 CPC low concentration analysis and results
(a) Counting efficiency curves based on CPC measurements. (b-e) CCN activation for 25, 50, 100, and 200 nm NaCl, respectively. (f) Critical supersaturation calculated for each activated fraction curve. (g) Apparent hygroscopicity for each case. (h) κ_{app} artifacts for each case.

Next, κ_{app} was calculated from theoretical critical supersaturations for each chosen diameter. To do so, four sigmoid curves representing sodium chloride CCN activation (hereon referred to as "activation curves") for 25, 50, 100, and 200 nm were generated. The κ-Köhler-derived critical supersaturation of sodium chloride was used as the midpoint of each activation curve, and one-tenth of this value was used as the standard deviation (100 % CE, Fig. 5b-e). These values are consistent with the standard deviation/midpoint ratio observed from our instrument's ammonium sulfate CCN calibration data.

Activation curves were then generated for CPC Cases 1-6 by dividing the activated fraction for each dry particle diameter by the counting efficiency for that diameter. Critical supersaturation was determined for each CPC case. Results are summarized in Fig. 5f. Next, critical supersaturation was converted to saturation, and $\kappa_{app,theory}$ was calculated for each diameter in each CPC Case using Eq. (4) (see Fig. 5g). As above, κ_{app} artifacts were calculated by finding the difference between these results and the literature value of κ_{app} for sodium chloride (see Fig. 5h).

For the diameters studied, the effect of maximum counting efficiency on CPC concentration (and activated fraction) is greater than the effect of 50 %-cut-off diameter. However, neither characteristic resulted in large κ_{app} artifacts. The largest κ_{app} artifact observed at "low" concentrations was 0.035 for CPC Case 4, 2.4 % of the literature value for the apparent hygroscopicity factor for sodium chloride.

4.2 CPC Operation at High Concentration

Operation at high concentrations introduces an additional source of undercounting through particle coincidence at the CPC optical counter. For the TSI 3010 CPC, undercounting is observed is for particle concentrations above $1 \times 10^4\ cm^{-3}$. At $5 \times 10^4\ cm^{-3}$, the detector saturates and cannot detect higher concentrations. By comparison, the TSI 3025 is effective at

counting higher particle concentrations, of up to $2.5 \times 10^4\ cm^{-3}$ (Hameri, O'Dowd, and Hoell 2002, Sem 2002).

To model undercounting due to particle coincidence, four CPC counting curves (Fig. 6a) were generated using the equations in Table 4. Case 7 represents a CPC where counting efficiency decreases with particle concentration, without reaching saturation. Cases 8-10 represent CPCs were saturation is reached at $4 \times 10^4\ cm^{-3}$, $2 \times 10^4\ cm^{-3}$, and $1 \times 10^4\ cm^{-3}$, respectively. These saturation concentrations are of similar magnitude to those observed from TSI 3010 concentration data.

In all cases, the aerosol population was assumed to be a distribution consisting of 5×10^6 particles/cm^3 with a peak concentration at 50 nm (Fig. 6b). Each case was applied to this theoretical distribution in order to determine the concentration measured by the CPC for 25, 50, 100 and 200 nm aerosols. Then, the counting efficiency was calculated for each case and aerosol diameter.

Table 4 Equations used to model the relationship between a reference or "true" aerosol concentration x, and the concentration measured by a condensation particle counter y

Case	Equation
CPC 7	$y = x - 2 \times 10^{-6} x^2$
CPC 8	$y = 40000\ \mathrm{erf}\left(\frac{x}{32000\sqrt{2}}\right)$
CPC 9	$y = 20000\ \mathrm{erf}\left(\frac{x}{16000\sqrt{2}}\right)$
CPC 10	$y = 10000\ \mathrm{erf}\left(\frac{x}{8000\sqrt{2}}\right)$

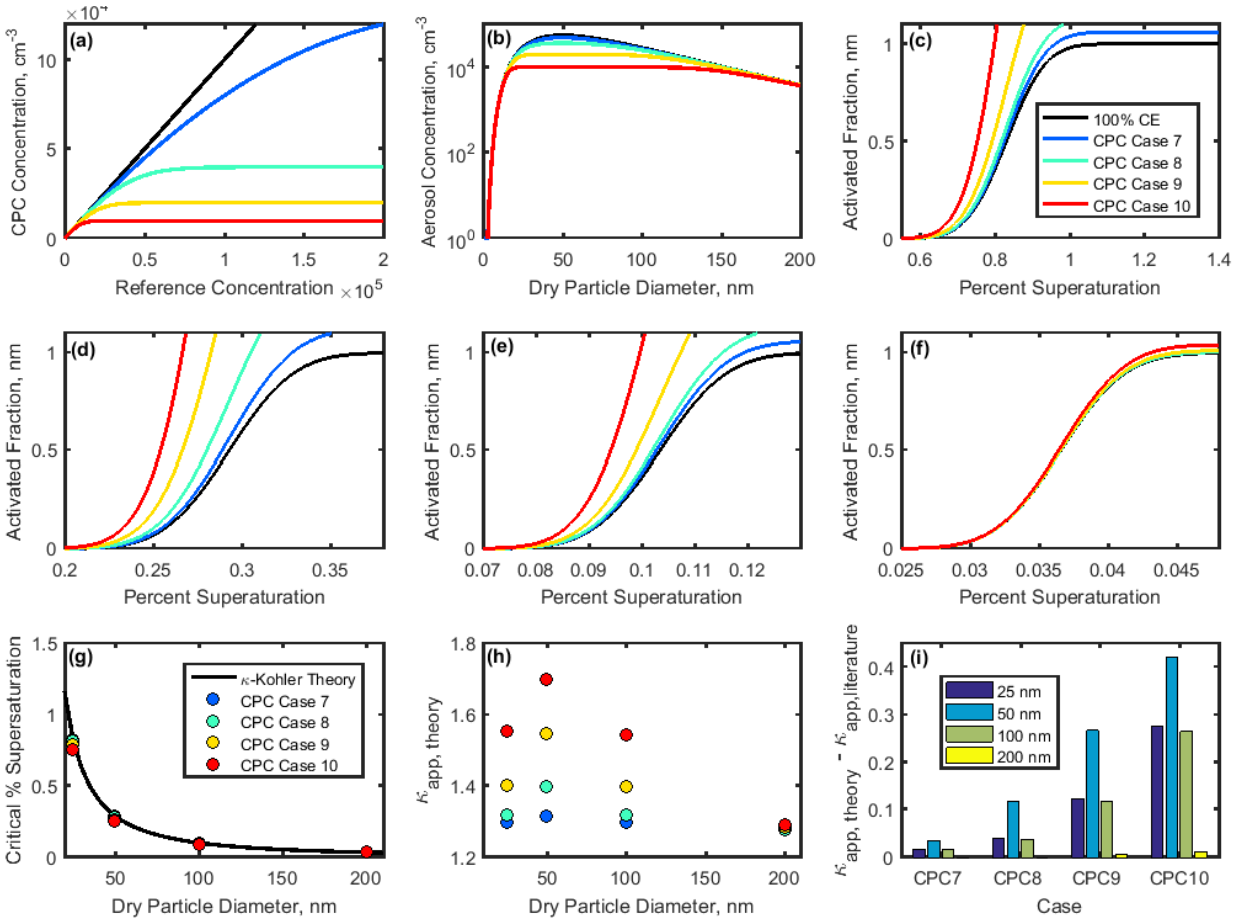

Figure 6 CPC high concentration analysis and results
(a) Theoretical relationships between the reference aerosol concentration and CPC concentration. (b) Concentration-dependent counting efficiencies were applied to a theoretical aerosol distribution. The ideal case (100 % counting efficiency), shown in black, is a lognormal distribution centered at 50 nm, consisting of 5 x 10^6 total particles. (c-f) Activated fraction for 25, 50, 100, and 200 nm NaCl aerosol, respectively. (g,h) Critical supersaturation and apparent hygroscopicity for each concentration-dependent case. (i) κ_{app} artifacts for each case.

Sigmoidal activated fraction curves were generated for 25, 50, 100 and 200 nm sodium chloride aerosols. As in the low concentration cases, the midpoint of each 100 % CE curve was chosen to be equal to the κ-Köhler-derived critical supersaturation of sodium chloride at each dry diameter, and the standard deviation of each curve is equal to one-tenth of the critical supersaturation.

These activated fraction curves were adjusted using the counting efficiencies calculated in the previous step. In cases where the activated fraction has increased due to undercounting by the CPC, the theoretical sigmoidal curve shifts to the left relative to the 100 % CE case (Fig. 6c-f). Thus, undercounting by the CPC effectively increases the reported activated fraction. As above, critical supersaturation was determined from each of these curves, and $\kappa_{app,theory}$ was subsequently calculated using Eq. (4) (Fig. 6g-h).

$\kappa_{app,theory}$ fell over a much wider range for 25, 50, and 100 nm particles (1.30-1.56, 1.32-1.70, and 1.30-1.55, respectively) than for 200 nm particles (1.28-1.29) due to the lower concentration of 200 nm particles in the chosen aerosol distribution, which resulted in a higher counting efficiency for these aerosols. In comparison, the largest range in $\kappa_{app,theory}$ was observed for 50 nm aerosols, the peak diameter in this aerosol distribution.

A wider range in $\kappa_{app,theory}$ was observed for the high-concentration CPC Cases (7-10) compared to the low-concentration CPC Cases (1-6). The lowest counting efficiency observed across the low-concentration cases was 89.9 % for 25 nm aerosol in Case 4, while the lowest counting efficiency observed in the high-concentration cases was 18.0 % for 50 nm aerosol in Case 10.

Artifacts in the apparent hygroscopicity parameter are shown in Fig. 6i. κ_{app} artifacts were the greatest for a CPC that becomes saturated at 20,000 particles/cm^3 ($0.0131 \leq \kappa_{app} \leq 0.4206$). The lower the concentration at which a CPC becomes saturated, the more quickly its counting

efficiency will drop as concentration increases, resulting in increased activated fraction and increased apparent hygroscopicity. The magnitude of artifacts due to CPC undercounting depends on the saturation concentration of the CPC and the distribution of the aerosol population being studied.

5. ARTIFACTS DERIVED FROM CLOUD CONDENSATION NUCLEI INSTRUMENTS

Finally, the third instrument whose performance accuracy contributes to the overall certainty in CCN assessment in the CCN instrument itself. Several instruments have been implemented for measuring CCN concentrations over the last few decades. Older models include the Continuous Flow Parallel Plate Diffusion Chamber (Sinnarwalla 1973) and the Hudson CCN spectrometer (Hudson 1989) which both employ an applied temperature gradient perpendicular to the aerosol flow. Newer models, such as the widely-used Droplet Measurement Technology Cloud Condensation Nuclei Counter (DMT CCN-100), operate with a streamwise temperature gradient and continuous, laminar flow (Lance et al. 2006). The following analysis considers the DMT CCN-100. According to the CCN-100 manual, the counting efficiency for this CCN instrument depends on concentration and supersaturation (Fig. 6a). The counting efficiency decreases rapidly with concentration at < 0.2 % SS due to rapid water vapor depletion at these low supersaturations, and falls off more slowly for > 0.2 % SS (DMT CCN-100 manual).

The counting efficiency of the DMT CCN-100 was tested for four lognormal aerosol distributions with peak concentrations at 50 nm and varying total concentrations (Table 5, Fig. 7b). Note that for comparison, CCN Case 1 was chosen to be identical to the aerosol distribution used for the high-concentration CPC cases. CCN Cases 2-4 follow the same distribution shape, with decreased total particle concentration.

Table 5 Total concentrations used in theoretical aerosol distribution for CCN-derived κ_{app} artifacts

Case	Total Concentration (particles/cm^3)
CCN 1	5×10^6
CCN 2	1×10^5
CCN 3	1×10^4
CCN 4	2×10^3

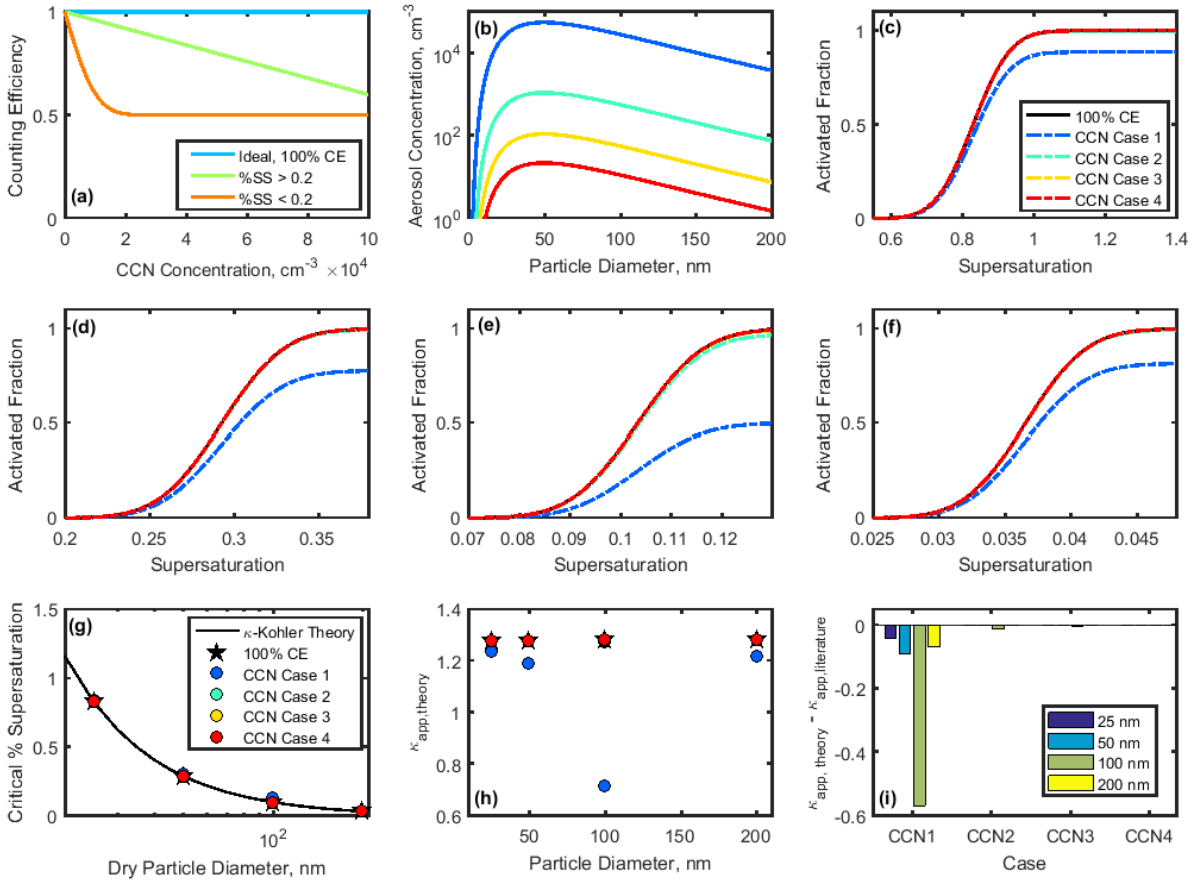

Figure 7 CCN analysis and results
(a) Counting efficiency of the DMT CCN-100. (b) Lognormal distributions used to study CCN undercounting at high concentrations. (c-f) Activation fractions for 25-200 nm NaCl particles, respectively. Supersaturation-specific counting efficiencies from (a) were applied to theoretical sigmoid curves for NaCl CCN activation. Activated fraction in the case of 100 % counting efficiency is shown for comparison. (g) Critical supersaturation for each case. (h) κ_{app} calculated for each case. (i) κ_{app} artifacts for each case.

The counting efficiencies for each case were applied to theoretical sodium chloride sigmoidal activated fraction curves to produce normalized activated fraction curves (Fig. 7c-f). As above, the midpoint is set to the critical supersaturation of sodium chloride at each dry diameter, and the standard deviation is assumed to be one-tenth of the critical supersaturation. CCN undercounting effectively decreases activated fraction, therefore shifting the activated fraction curve downwards and towards higher percent supersaturations. The opposite effect is observed when CPC undercounting occurs. Critical supersaturation was determined for each CCN case, as above (Fig. 7g). Values of SS_{crit} were then converted to saturation, and $\kappa_{app,theory}$ was calculated using Eq. (4) (Fig. 7h).

Significant deviations from κ-Köhler theory were only observed in CCN Case 1, with total aerosol concentration 5×10^6 particles/cm^3 (Fig. 7g-i). The largest deviation for CCN Case 1 was observed in 100 nm particles ($\kappa_{app,artifact} = -0.57$), due to the higher concentration of 100 nm particles compared to 25 and 200 nm particles, and the lower supersaturation necessary for activation. The largest artifacts across CCN Cases 2 and 3 were also observed for 100 nm particles, though no artifacts were observed for any particle diameter in CCN Case 4 due to the much lower concentrations.

Sodium chloride is very hygroscopic. It should be noted that aerosols consisting of less hygroscopic compounds will activate at higher supersaturations (> 0.2 % SS regime) which will lead to smaller κ_{app} artifacts when the same aerosol distribution and total aerosol concentration is considered. If a mixture was considered (for example, sodium chloride with a non-hygroscopic species such as soot) the results may also be different. The shape of the aerosol

distribution must also be taken into account. A distribution with a narrower peak than the one generated for this analysis would be at risk for larger κ_{app} artifacts for any total aerosol concentration, and these artifacts would be greater at the peak diameter, while a broader distribution would result in less variation in κ_{app} artifacts for each particle diameter.

6. RESULTS

A comparison of several instrument sources of error in CCN-derived κ_{app} is shown in Fig. 8. DMA Case 4, CPC Case 4, CPC Case 10, and CCN Case 1 represent the operating conditions that resulted in the largest κ_{app} artifacts in this study. In DMA Case 4, the aerosol/sheath ratio of 0.30 resulted in a broadened aerosol distribution downstream of the DMA. Compared to DMA Case 1, where $Q_a/Q_{sh} = 0.10$, the downstream diameter range in DMA Case 4 was 300 % higher for 25 nm particles, resulting in a spread of 20-36 nm. Similarly, the diameter ranges for 50, 100, and 200 nm diameter were 220 %, 230 %, and 220 % wider than in Case 1, respectively. Compared to the most ideal DMA case presented in this study (DMA Case 2), where $Q_a/Q_{sh} = 0.05$, the downstream diameter range in DMA Case 4 was 700 % higher for 25 nm particles; the diameter ranges for 50, 100, and 200 nm diameter were 540 %, 560 %, and 520 % wider than in Case 2, respectively.

CPC Case 4 represents κ_{app} artifacts (0.031-0.035) due to undercounting that arises from poor maximum CPC counting efficiency (90 %), which may be observed when using butanol as a working fluid while measuring the concentration of inorganic aerosols. In contrast, κ_{app} artifacts are negligible (< 0.10 % of κ_{app}^{NaCl}) in CPC Case 3, where maximum counting efficiency = 100 %. CPC Cases 8 and 10 represent undercounting at high concentration with CPCs where saturation is observed at $4 \times 10^4 cm^{-3}$ and $1 \times 10^4 cm^{-3}$, respectively. Counting efficiency drops off more rapidly with concentration in the latter case, resulting in κ_{app} artifacts that are

highest at the peak of the aerosol distribution (0.1190 and 0.4206 for 50 nm aerosols in CPC Cases 8 and 10, respectively).

CCN Case 1 represents CCN undercounting at high concentration (total aerosol concentration = $5 \times 10^6 cm^{-3}$). CCN undercounting is greatest for low supersaturation (< 0.2 %) and high concentration, resulting in the lowest counting efficiency and highest κ_{app} artifacts (- 0.57) for 100 nm aerosols in CCN Case 1. The largest CCN-derived κ_{app} artifact observed outside of CCN Case 1 was – 0.01 for 100 nm aerosols in CCN Case 2.

The combined artifacts for the cases where the highest artifacts were observed (DMA Case 4, CPC Case 4, CPC Case 10, CCN Case 1) are 0.21, 0.24, 0.32, and 0.21 for 25, 50, 100, and 200 nm particles respectively, as shown in Fig. 8. The combined artifacts for the lowest-artifact cases (DMA Case 2, CPC Case 3, and CCN Case 4) are < 0.001 except for 200 nm particles, where $\kappa_{app,artifact}$ = 0.0013.

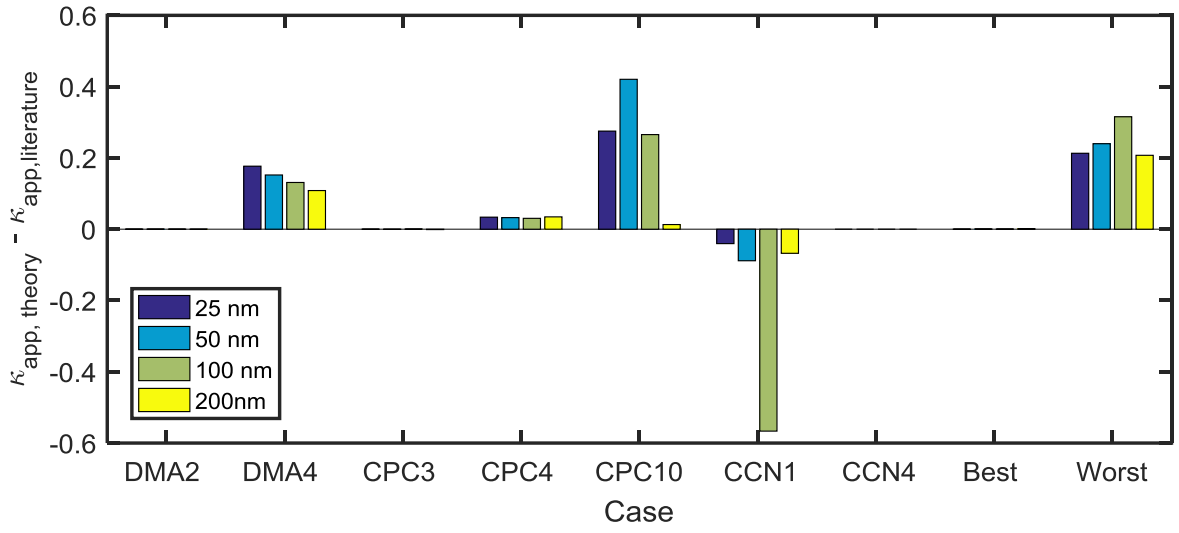

Figure 8 Comparison of κ_{app} artifacts from best and worst cases
Combined artifacts for the lowest-artifact cases (Best: DMA Case 2, CPC Case 3, and CCN Case 4) and the highest-artifact cases (Worst: DMA Case 4, CPC Case 4, CPC Case 8, and CCN Case 1). All results are from sodium chloride aerosol.

7. DISCUSSION

The sensitivity of weather and climate models to accuracy in CCN activation predictions has been demonstrated in other works (Karydis et al. 2012, Kawecki and Steiner 2018, Liu and Wang 2010). Possible sources of apparent hygroscopicity artifacts calculated from CCN measurements have been presented in this study. This analysis has focused on sodium chloride and ammonium sulfate aerosols, but it can be extended to other aerosol populations, including mixtures and field samples.

The largest artifacts ($-0.57 < \kappa_{app,artifact} < 0.42$) in this study arise from undercounting by condensation particle counters and cloud condensation nuclei counters at high concentration. This problem arises in cases which represent attempts to measure aerosol concentrations much higher than are recommended for these instruments, ~10^4 cm^{-3} (CPC Cases 7-10 and CCN Case 4). Corrective action should be taken to dilute aerosol samples in order to avoid undercounting.

Smaller artifacts ($\kappa_{app,artifact} < 0.04$) were observed for the CPC cases where 50 %-cut-off diameter and maximum counting efficiency were varied. Given the chosen particle diameters (25, 50, 100, 200 nm), κ_{app} artifacts due to d_{50} were minimal. The largest κ_{app} artifacts for a CPC counting at low concentration (0.031-0.035) were observed where the maximum counting efficiency was equal 0.90. This may represent a compositional mismatch between n-butanol as the working fluid and sodium chloride as the aerosol, due to the poor solubility of the latter in the former. Individual n-butanol CPCs may exhibit higher maximum counting efficiencies for sodium chloride.

Uncertainty arising from the DMA depended greatly on the chosen aerosol and sheath settings. One set of DMA cases (Cases 2-4) examined the effect of aerosol/sheath ratio. By decreasing this ratio, a narrower near-monodisperse flow can be produced, which increases the accuracy of calculated κ_{app}. The κ_{app} artifacts for an aerosol/sheath ratio of 0.10 were 1.1 % of $\kappa_{literature}$ for 25 nm sodium chloride aerosols, 0.93 % for 50 nm, 0.81 % for 100 nm, and 0.66 % for 200 nm. Decreasing the aerosol/sheath ratio to 0.05 resulted in $\kappa_{app} \approx 0.01$ % of $\kappa_{literature}$ for NaCl. When a ratio of 0.30 was employed, the resulting artifacts that were ~10 % of $\kappa_{literature}$ for sodium chloride.

The second set of DMA cases (5-7) were designed to evaluate the effects of holding the sheath flow constant while varying the excess air flow by -2 %, +2 %, and +5 %. These resulted in shifts of ≤ 2 nm for 25 nm and 50 nm particles, ≤ 4 nm for 100 nm particles, and ≤ 7 nm for 200 nm particles. The downstream aerosol distribution was shifted towards larger particle diameters when sheath flow exceeded excess flow, and towards smaller particle diameter when sheath flow was less than excess flow. When taking field measurements, the composition of the sample may vary with particle diameter, thereby introducing another source of error from a broader DMA distribution.

Under optimal operating conditions, where the DMA sample/sheath ratio is 0.10 and excess/sheath ratio is 1.0, and in the absence of undercounting by the CPC or CCN, uncertainties

in κ_{app} are within ±1.1 % for 25 to 200 nm aerosols. When the DMA sample/sheath ratio drops to 0.05, κ_{app} uncertainties decrease to ±0.01 %.

Apparent hygroscopicity parameter artifacts were calculated for two pure, inorganic species in this study. This analysis could be used to estimate κ_{app} artifacts for ambient aerosol populations, which may result in a better understanding of the "real' differences between these populations. As discussed in the introduction, Collins et al. 2016 aggregated κ_{app} from several mesocosm and field studies for 30-100 nm sea spray aerosol ($0.4 < \kappa_{app}^{SSA} < 1.3$). The wide range of κ_{app} in these studies may be attributed to differences in composition, experimental artifacts, or a combination of the two. Quantification of experimental artifacts would facilitate interpretation of κ_{app} in aerosol populations and constrain the importance of composition in CCN activation.

8. CONCLUSION

There has been a recent proliferation of CCN data availability from multiple researchers and multiple experimental setups. To maximize the utility of these studies and to compare cloud-activating properties of various ambient aerosol masses, it is essential that artifacts are considered in both CCN data collection and in reporting of the data.

REFERENCES

Asa-Awuku, A., A. Nenes, S. Gao, R. C. Flagan, and J. H. Seinfeld. 2010. "Water-soluble SOA from Alkene ozonolysis: composition and droplet activation kinetics inferences from analysis of CCN activity." *Atmospheric Chemistry and Physics* 10 (4):1585-1597. doi: 10.5194/acp-10-1585-2010.

Barmpounis, K., A. Maisser, A. Schmidt-Ott, and G. Biskos. 2016. "Lightweight differential mobility analyzers: Toward new and inexpensive manufacturing methods." *Aerosol Science and Technology* 50 (1):4. doi: 10.1080/02786826.2015.1130216.

Betancourt, R. M., and A. Nenes. 2014. "Understanding the contributions of aerosol properties and parameterization discrepancies to droplet number variability in a global climate model." *Atmospheric Chemistry and Physics* 14 (9):4809-4826. doi: 10.5194/acp-14-4809-2014.

Betancourt, R. M., A. Nenes, and X. H. Liu. 2013. "Relative Contributions of Aerosol Properties to Cloud Droplet Number: Adjoint Sensitivity Approach in a GCM." 19th International Conference on Nucleation and Atmospheric Aerosols (ICNAA), Colorado State Univ, Ctr Arts, Fort Collins, CO, Jun 23-28.

Brooks, Sarah D., and Daniel C.O. Thornton. 2018. "Marine Aerosols and Clouds." *Annual Review of Marine Sciences* 10:289-313.

Carrico, C. M., M. D. Petters, S. M. Kreidenweis, J. L. Collett, G. Engling, and W. C. Malm. 2008. "Aerosol hygroscopicity and cloud droplet activation of extracts of filters from biomass burning experiments." *Journal of Geophysical Research-Atmospheres* 113 (D8):9. doi: 10.1029/2007jd009274.

Carslaw, K. S., L. A. Lee, C. L. Reddington, K. J. Pringle, A. Rap, P. M. Forster, G. W. Mann, D. V. Spracklen, M. T. Woodhouse, L. A. Regayre, and J. R. Pierce. 2013. "Large contribution of natural aerosols to uncertainty in indirect forcing." *Nature* 503 (7474):67-+. doi: 10.1038/nature12674.

Chang, D. Y., J. Lelieveld, H. Tost, B. Steil, A. Pozzer, and J. Yoon. 2017. "Aerosol physicochemical effects on CCN activation simulated with the chemistry-climate model EMAC." *Atmospheric Environment* 162:127-140. doi: 10.1016/j.atmosenv.2017.03.036.

Clegg, S. L., P. Brimblecombe, and A. S. Wexler. 1998. "Thermodynamic model of the system H+-NH4+-SO42--NO3--H2O at tropospheric temperatures." *Journal of Physical Chemistry A* 102 (12):2137-2154. doi: 10.1021/jp973042r.

Collins, D. B., T. H. Bertram, C. M. Sultana, C. Lee, J. L. Axson, and K. A. Prather. 2016. "Phytoplankton blooms weakly influence the cloud forming ability of sea spray aerosol." *Geophysical Research Letters* 43 (18):9975-9983. doi: 10.1002/2016gl069922.

Crosbie, E., J. S. Youn, B. Balch, A. Wonaschutz, T. Shingler, Z. Wang, W. C. Conant, E. A. Betterton, and A. Sorooshian. 2015. "On the competition among aerosol number, size and composition in predicting CCN variability: a multi-annual field study in an urbanized desert." *Atmospheric Chemistry and Physics* 15 (12):6943-6958. doi: 10.5194/acp-15-6943-2015.

DeCarlo, P. F., J. G. Slowik, D. R. Worsnop, P. Davidovits, and J. L. Jimenez. 2004. "Particle morphology and density characterization by combined mobility and aerodynamic diameter measurements. Part 1: Theory." *Aerosol Science and Technology* 38 (12):1185-1205. doi: 10.1080/027868290903907.

Grimm Aerosol Technik. 2009. “Scanning Mobility Particle Sizer Series 5.400 and 5.500.” Ainring, Germany: Grimm Aerosol Technik.

Hameri, K., C. D. O'Dowd, and C. Hoell. 2002. "Evaluating measurements of new particle concentrations, source rates, and spatial scales during coastal nucleation events using condensation particle counters." *Journal of Geophysical Research-Atmospheres* 107 (D19):11. doi: 10.1029/2001jd000411.

Hartz, K. E. H., J. E. Tischuk, M. N. Chan, C. K. Chan, N. M. Donahue, and S. N. Pandis. 2006. "Cloud condensation nuclei activation of limited solubility organic aerosol." *Atmospheric Environment* 40 (4):605-617. doi: 10.1016/j.atmosenv.2005.09.076.

Heim, M., G. Kasper, G. Reischl, and C. Gerhart. 2004. "Performance of a New Commercial Electrical Mobility Spectrometer." *Aerosol Science and Technology* 38 (1):3-14. doi: 10.1080/02786820490519252.

Hermann, M., B. Wehner, O. Bischof, H. S. Han, T. Krinke, W. Liu, A. Zerrath, and A. Wiedensohler. 2007. "Particle counting efficiencies of new TSI condensation particle counters." *Journal of Aerosol Science* 38 (6):674-682. doi: 10.1016/j.jaerosci.2007.05.001.

Hudson, J. G. 1989. "An Instantaneous CCN Spectrometer." *Journal of Atmospheric and Oceanic Technology* 6 (6):1055-1065. doi: 10.1175/1520-0426(1989)006<1055:aics>2.0.co;2.

IPCC, 2013: Summary for Policymakers. In *Climate Change 2013: The Physical Science Basis. Contribution of Working Group 1 to the Fifth Assessment Report of the Intergovernmental Panel on Climate Change*, edited by T.F. Stocker, D. Qin, G.-K. Plattner, M. Tignor, S.K. Allen, J. Boschung, A. Nauels, Y. Xia, V. Bex and

P.M. Midgley Cambridge University Press: Intergovernmental Panel on Climate Change.

Jokinen, V., and J. M. Makela. 1997. "Closed-loop arrangement with critical orifice for DMA sheath excess flow system." *Journal of Aerosol Science* 28 (4):643-648. doi: 10.1016/s0021-8502(96)00457-0.

Karydis, V. A., S. L. Capps, A. G. Russell, and A. Nenes. 2012. "Adjoint sensitivity of global cloud droplet number to aerosol and dynamical parameters." *Atmospheric Chemistry and Physics* 12 (19):9041-9055. doi: 10.5194/acp-12-9041-2012.

Kawecki, S., and A. L. Steiner. 2018. "The Influence of Aerosol Hygroscopicity on Precipitation Intensity During a Mesoscale Convective Event." *Journal of Geophysical Research-Atmospheres* 123 (1):424-442. doi: 10.1002/2017jd026535.

Knutson, E. O., and K. T. Whitby. 1975. "Aerosol classification by electric mobility: apparatus, theory, and applications." *Journal of Aerosol Science* 6 (6):443-451. doi: https://doi.org/10.1016/0021-8502(75)90060-9.

Koehler, K. A., S. M. Kreidenweis, P. J. DeMott, A. J. Prenni, C. M. Carrico, B. Ervens, and G. Feingold. 2006. "Water activity and activation diameters from hygroscopicity data - Part II: Application to organic species." *Atmospheric Chemistry and Physics* 6:795-809. doi: 10.5194/acp-6-795-2006.

Kumar, P. P., K. Broekhuizen, and J. P. D. Abbatt. 2003. "Organic acids as cloud condensation nuclei: Laboratory studies of highly soluble and insoluble species." *Atmospheric Chemistry and Physics* 3:509-520.

Lance, S., J. Medina, J. N. Smith, and A. Nenes. 2006. "Mapping the operation of the DMT Continuous Flow CCN counter." *Aerosol Science and Technology* 40 (4):242-254. doi: 10.1080/02786820500543290.

Liu, X. H., and J. A. Wang. 2010. "How important is organic aerosol hygroscopicity to aerosol indirect forcing?" *Environmental Research Letters* 5 (4):10. doi: 10.1088/1748-9326/5/4/044010.

Mamakos, A., L. Ntziachristos, and Z. Sarnaras. 2007. "Diffusion broadening of DMA transfer functions. Numerical validation of Stolzenburg model." *Journal of Aerosol Science* 38 (7):747-763. doi: 10.1016/j.jaerosci.2007.05.004.

Mei, F., H. J. Fu, and D. R. Chen. 2011. "A cost-effective differential mobility analyzer (cDMA) for multiple DMA column applications." *Journal of Aerosol Science* 42 (7):462-473. doi: 10.1016/j.jaerosci.2011.04.001.

Moore, R. H., T. Raatikainen, J. M. Langridge, R. Bahreini, C. A. Brock, J. S. Holloway, D. A. Lack, A. M. Middlebrook, A. E. Perring, J. P. Schwarz, J. R. Spackman, and A. Nenes. 2012. "CCN Spectra, Hygroscopicity, and Droplet Activation Kinetics of Secondary Organic Aerosol Resulting from the 2010 Deepwater Horizon Oil Spill." *Environmental Science & Technology* 46 (6):3093-3100. doi: 10.1021/es203362w.

Ovadnevaite, J., D. Ceburnis, G. Martucci, J. Bialek, C. Monahan, M. Rinaldi, M. C. Facchini, H. Berresheim, D. R. Worsnop, and C. O'Dowd. 2011. "Primary marine organic aerosol: A dichotomy of low hygroscopicity and high CCN activity." *Geophysical Research Letters* 38:5. doi: 10.1029/2011gl048869.

Petters, M. D., and S. M. Kreidenweis. 2007. "A single parameter representation of hygroscopic growth and cloud condensation nucleus activity." *Atmospheric Chemistry and Physics* 7 (8):1961-1971. doi: 10.5194/acp-7-1961-2007.

Petters, M. D., and S. M. Kreidenweis. 2013. "A single parameter representation of hygroscopic growth and cloud condensation nucleus activity - Part 3: Including surfactant partitioning." *Atmospheric Chemistry and Physics* 13 (2):1081-1091. doi: 10.5194/acp-13-1081-2013.

Rogers, R.R., and M.K. Yau. 1989. *A Short Course In Cloud Physics*, edited by D. Ter Haar, 87-89. Tarrytown, New York, USA: Elsevier Science Inc.

Rose, D., S. S. Gunthe, E. Mikhailov, G. P. Frank, U. Dusek, M. O. Andreae, and U. Poschl. 2008. "Calibration and measurement uncertainties of a continuous-flow cloud condensation nuclei counter (DMT-CCNC): CCN activation of ammonium sulfate and sodium chloride aerosol particles in theory and experiment." *Atmospheric Chemistry and Physics* 8 (5):1153-1179. doi: 10.5194/acp-8-1153-2008.

Schmale, J., S. Henning, S. Decesari, B. Henzing, H. Keskinen, K. Sellegri, J. Ovadnevaite, M. L. Pohlker, J. Brito, A. Bougiatioti, A. Kristensson, N. Kalivitis, I. Stavroulas, S. Carbone, A. Jefferson, M. Park, P. Schlag, Y. Iwamoto, P. Aalto, M. Aijala, N. Bukowiecki, M. Ehn, G. Frank, R. Frohlich, A. Frumau, E. Herrmann, H. Herrmann, R. Holzinger, G. Kos, M. Kulmala, N. Mihalopoulos, A. Nenes, C. O'Dowd, T. Petaja, D. Picard, C. Pohlker, U. Poschl, L. Poulain, A. S. H. Prevot, E. Swietlicki, M. O. Andreae, P. Artaxo, A. Wiedensohler, J. Ogren, A. Matsuki, S. S. Yum, F. Stratmann, U. Baltensperger, and M. Gysel. 2018. "Long-term cloud condensation nuclei number concentration, particle number size distribution and chemical composition measurements

at regionally representative observatories." *Atmospheric Chemistry and Physics* 18 (4):2853-2881. doi: 10.5194/acp-18-2853-2018.

Sem, G. J. 2002. "Design and performance characteristics of three continuous-flow condensation particle counters: a summary." *Atmospheric Research* 62 (3-4):267-294. doi: 10.1016/s0169-8095(02)00014-5.

Seol, K. S., Y. Tsutatani, R. P. Camata, J. Yabumoto, S. Isomura, Y. Okada, K. Okuyama, and K. Takeuchi. 2000. "A differential mobility analyzer and a Faraday cup electrometer for operation at 200-930 Pa pressure." *Journal of Aerosol Science* 31 (12):1389-1395. doi: 10.1016/s0021-8502(00)00037-9.

Sinnarwalla, A.M. and Alofs, D.J. 1973. "A Cloud Nucleus Counter with Long Available Growth Time." *Journal of Applied Meteorology* (12):831-835.

Stratmann, F., T. Kauffeldt, D. Hummes, and H. Fissan. 1997. "Differential electrical mobility analysis: A theoretical study." *Aerosol Science and Technology* 26 (4):368-383. doi: 10.1080/02786829708965437.

Sullivan, R. C., M. J. K. Moore, M. D. Petters, S. M. Kreidenweis, G. C. Roberts, and K. A. Prather. 2009. "Timescale for hygroscopic conversion of calcite mineral particles through heterogeneous reaction with nitric acid." *Physical Chemistry Chemical Physics* 11 (36):7826-7837. doi: 10.1039/b904217b.

Svenningsson, B., J. Rissler, E. Swietlicki, M. Mircea, M. Bilde, M. C. Facchini, S. Decesari, S. Fuzzi, J. Zhou, J. Monster, and T. Rosenorn. 2006. "Hygroscopic growth and critical supersaturations for mixed aerosol particles of inorganic and organic compounds of atmospheric relevance." *Atmospheric Chemistry and Physics* 6:1937-1952. doi: 10.5194/acp-6-1937-2006.

APPENDIX

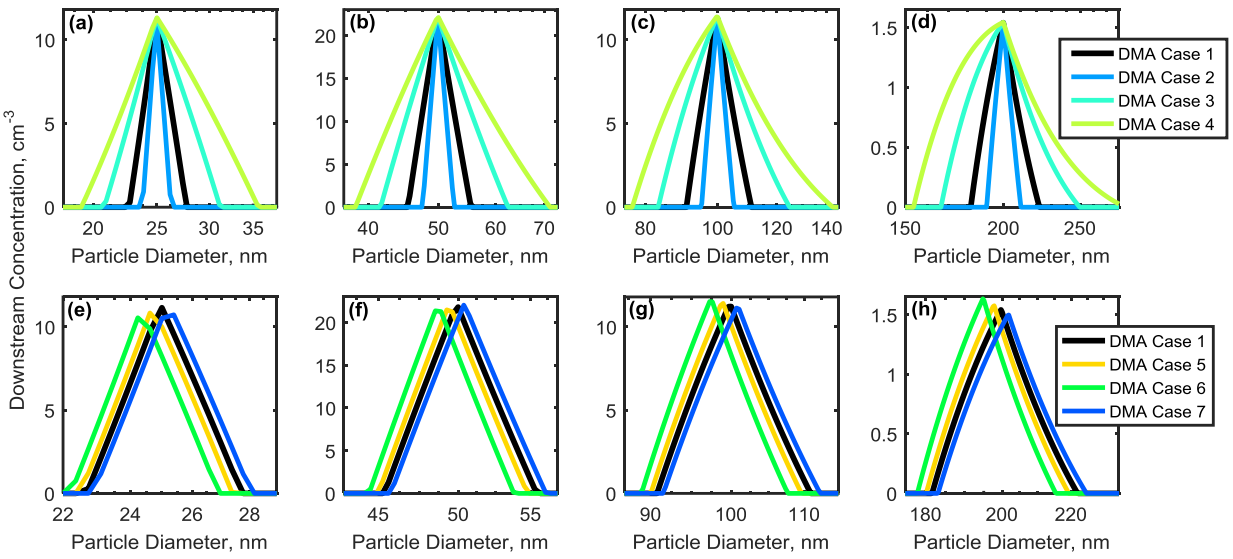

Figure A-1 (a-d) Downstream aerosols concentrations, cm^{-3}, for DMA Cases 1-4, with sheath and excess air flow 3 L min^{-1}, and aerosol and sample flow of 0.06-0.90 L min^{-1}. (e-h) Downstream concentrations for DMA Cases 1 and 5-7, with sheath air flow 3.0 L min^{-1}, sample flow 0.30 L min^{-1}, and excess air flow 2.94-3.06 L/min.